Nanoscale

Accepted Manuscript

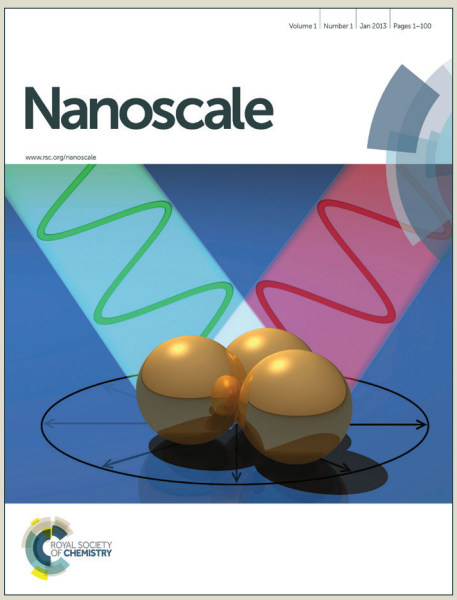

ROYAL SOCIETY OF CHEMISTRY

www.rsc.org/nanoscale

Journal Name

RSCPublishing

COMMUNICATION

{116} faceted anatase single-crystalline nanosheet arrays: facile synthesis and enhanced electrochemical performances

Cite this: DOI: 10.1039/x0xx00000x

Feng Li,[a] Xiaoning Li,[a] Ranran Peng,[ac] Xiaofang Zhai,[bc] Shangfeng Yang,[ac] Zhengping Fu,*[ac] and Yalin Lu*[abc]

Received 00th January 2014,
Accepted 00th January 2014

DOI: 10.1039/x0xx00000x

www.rsc.org/

Single-crystalline anatase TiO_2 nanosheet arrays were synthesized on a transparent conductive fluorine-doped tin oxide (FTO) substrate with a unique one-step alcohol-thermal process. The nanosheets were nearly vertically grown on the FTO substrate along their <1 $\bar{1}$ 0> zone, and they were dominated by {116} facets. The as-fabricated {116} faceted single-crystalline anatase nanosheet arrays exhibit a much higher reduction capacity and a much better electrochemical reversibility than both {001} faceted anatase single-crystalline nanosheet arrays and P25 film. The results indicate a promising application potential for the new material in the photoelectrochemical field.

Introduction

Nanostructured TiO_2 films or arrays with a large percentage of reactive facets are preferred for potential applications in electrocatalysis, sensors, hydrogen production, lithium batteries, dye-sensitized solar cells, and so on.[1-5] However, past synthesized anatase TiO_2 crystals are usually dominated by the less reactive {101} facets, because that facets with high reactivity will normally diminish during the crystal growth process as a result of the minimization requirement of the surface energy. Recently, Taketo Taguchi and coworkers generated new crystalline faces on both anatase and rutile TiO_2 particles by means of chemical etching in aqueous hydrofluoric acid and in hot sulfuric acid via the 'top-down' approach.[6] Yang et al. also successfully synthesized anatase TiO_2 single crystals that exposed with {001} facets by using hydrofluoric acid as the capping agent via the 'bottom up' approach.[7] Following these works, extensive past efforts have been devoted to synthesize various types of anatase TiO_2, mainly exposed with the reactive facets of {001} and {100}.

In contrast to the extensive past effort on developing anatase TiO_2 exposed with low Miller-index facets like {101}, {001}, and {100}, much less work has been done so far on developing anatase TiO_2 exposed with high Miller-index facets, though high Miller-index facets may have unique and improved electrochemical properties. Recently, Wu et al. synthesized asymmetric anatase TiO_2 nanocrystals with a bipyramidal structure bound by {201} and {401} facets, which exhibited a low initial irreversible capacity loss and a good cycle capacity retention in potential lithium-ion battery applications.[8] In our previous work, anatase TiO_2 nanosheet arrays, in which each large nanosheet was polycrystalline and was assembled by very tiny TiO_2 nanocrystals with their exposed {116} facets parallel to the large nanosheet's surface, were synthesized via a two-step toluene-thermal process. The arrays exhibited a 50% higher photocatalytic activities than that in the {001} facets oriented nanosheet arrays.[9] Importantly, it should be pointed out here that the nanosheets inside the array are polycrystalline, assembled by smaller {116} faceted nanoparticles via a proposed 'oriented attachment' mechanism. In fact, large single-crystalline anatase TiO_2 nanosheets arrays grown directly on transparent conducting substrates, potentially with both light-trapping effect and improved electron transporting properties, are highly desired for future photoelectronic applications.[10-13] Indeed, it is still a big challenge to synthesize such large TiO_2 nanosheets, which should be single-crystalline and are exposed with a large percentage of high Miller-index facets, such as the {116} facets.

In this work, an improved one-step alcohol-thermal route was firstly taken to synthesize the anticipated new anatase TiO_2 arrays directly on the FTO substrate, in which hydrofluoric acid with high relative concentration will act as a hydrolysis monitor and a capping agent. The large-area film array was indeed assembled by the {116} faceted single-crystalline anatase nanosheets. The new nanosheet arrays showed both enhanced anti-reflection performance and the improved electrochemical properties, which may originate from the light-trapping nature of the array structure and from the exposed {116} facets, intrinsically more reactive. Possible mechanism for the {116} faceted single-crystalline nanosheet has also been discussed following the time-dependent serial experiments during the synthesis.

Experimental section

In a typical synthesis, the FTO coated glass substrate was ultrasonically cleaned sequentially in acetone, ethanol, and distilled water, each for 15 min, and was then immersed in a 1 M NaOH aqueous solution for 24 h. It was then rinsed with distilled water, and was finally dried in the air. A TiO_2 seed layer was prepared on the as-cleaned FTO coated glass by the spin coating method. The reference P25 film was also prepared on the FTO coated glass through the similar approaches discussed before.

Synthesis of {116} faceted anatase single-crystalline nanosheets array (STNA-116)

0.5 ml of titanium butoxide was added dropwise to 15 ml of ethanol, and then the mixture was stirred at the ambient condition for 5 min before the addition of 0.5 ml of hydrofluoric acid. After stirring for another 5 min, the mixture was transferred to a dried 50 ml Teflon-lined autoclave within a piece of FTO coated glass substrate placed vertically, and kept at 200 ºC for 12 h. After the synthesis, the FTO substrate was then taken out, washed with ethanol and distilled water, then fully dried in air.

In order to study the growth mechanism, serial STNA-116 samples were synthesized through the same route, with doubled precursor concentration and a series of the used growth times (2, 4, 8, 12, 16 h).

Synthesis of {001} faceted anatase single-crystalline nanosheets array (STNA-001)

3.0 ml of titanium butoxide was added dropwise to 20 ml of toluene, and then the mixture was stirred at the ambient condition for 5 min before the addition of 1.2 ml of hydrofluoric acid. After stirring for another 5 min, the mixture was transferred to a dried 50 ml Teflon-lined autoclave within a piece of FTO coated glass substrate placed vertically, and kept at 180 ºC for 24 h. After the synthesis, the FTO substrate was taken out, washed with ethanol and distilled water, then fully dried in air.

Characterization

X-ray diffraction patterns were obtained by using a TTR-III X-ray diffractometer with Cu Kα radiation (λ =1.5418Å). The morphology of the fabricated sample was examined by FESEM (JSM-6700F) and TEM (JEM-2011). Reflectance spectra were tested by a UV-Vis spectrophotometer (SOLID 3700). Electrochemical performance of the nanosheet arrays was measured in a three-electrode electrochemical cell with the electrochemical workstation (CHI660E, Shanghai Chenhua Device Company, China), a Pt wire as a counter electrode and an Ag/AgCl (saturated KCl) as the reference electrode dipped in a solution of 0.5 M H_2SO_4 (scan rate: 50 mV s^{-1}).

Results and discussion

As shown in Fig. S1†, the STNA-116 samples are uniform in an area as large as 2.2 cm x 2.0 cm. The field emission scanning electron microscopy (FESEM) shows that the fishnet-like-structured array consists of nanosheets with a side length of about 2.55 μm and a laminar thickness of 25-30 nm. Crossed nanosheets marked with circles in Fig. 1b may be attributed to the nucleation and growth at defects including line dislocations generated from the growth process. As shown and marked in Fig. 1c and d, the fishnet-like structures start from the substrate and the nanosheets are nearly perpendicular to the FTO substrate. This can be attributed to the crossed growths and to the supporting mutually on each other (Fig. 1a and b), keeping the nanosheets from further aggregating or collapsing. As manifested by the FESEM images, the STNA-116 shows a much smoother top surface than the STNA-001 (Fig. S2†), which should be more beneficial for further device fabrications.

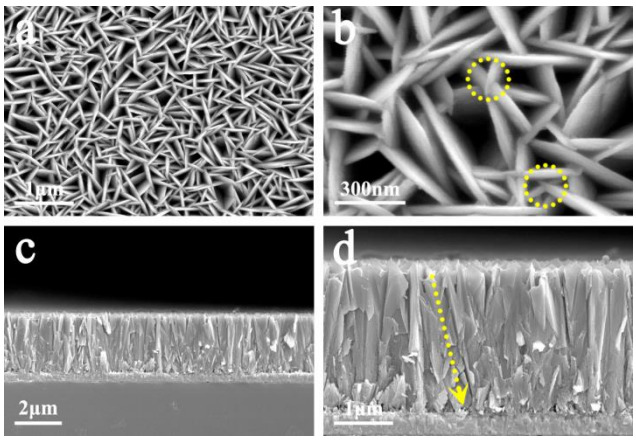

Fig. 1 FESEM images of STNA-116 grown on FTO substrate in 15 ml ethanol, 0.5 ml titanium butoxide, and 0.5 ml hydrofluoric acid at 200 °C for 12 h. (a, b) Top views with different magnifications, (c, d) cross-sectional views with different magnifications.

The crystalline structure of the nanosheet arrays was studied by X-ray Diffraction (XRD). As shown in Fig. 2a, all of the indicated diffraction peaks can be attributed to the anatase TiO_2 (Fig. 2d, JCPDF no. 89-4921, a=b=0.3777 nm, c=0.9501 nm) and to the FTO substrate (Fig. 2c). As indicated by the relative intensity of the diffraction peaks from the FTO substrate and by the enlarged XRD patterns shown in Fig. S3†, the diffraction peak at about 37.8° originated mainly from the FTO substrate. Compared to the diffraction pattern from STNA-001, the (220) and (211) peaks of the STNA-116 were significantly enhanced, while the (101) peak was greatly weakened, indicating that the nanosheets in STNA-116 are highly oriented. It is reasonable for us to

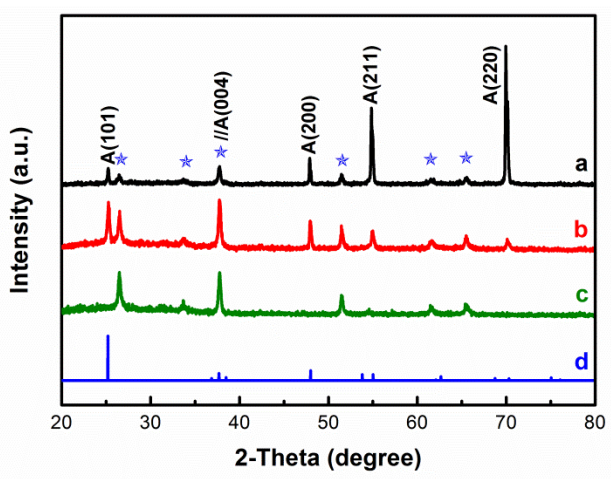

Fig. 2 XRD patterns of (a) STNA-116 and (b) STNA-001 grown on FTO substrate, (c) FTO substrate and (d) anatase TiO_2 (JCPDF no.89-4921). The reflection marked with star is ascribed to the FTO substrate.

suggest that the nanosheets may grow from the substrate along the <110> zones, which are perpendicular to the {220} lattice planes. Furthermore, the $\{2\,\bar{1}\,\bar{1}\}$ and $\{2\,\bar{2}\,0\}$ lattice plane of anatase TiO_2 are almost orthogonal to the {116} plane, the enhanced (220) and (211) diffraction peaks suggesting that the nanosheets are exposed with {116} facets (as a result, the (116) diffraction peak was absent due to the vertically aligned nanosheets). The XRD pattern of STNA-116 in our work is also distinctively different from the TiO_2 nanosheet array exposed with {001} facets in those previous reports,[14, 15] indicating a quite different nanostructures between them.

TEM was adopted to further investigate the crystallinity of the nanosheets in STNA-116. The sample in Fig. 3a is actually a stacking of a few nanosheets, mainly caused by the HRTEM sample preparation procedure. During the TEM test procedure, the nanosheets were carefully adjusted in order to be perpendicular to the incident electron beam. Uniform contrasts separated by the clear edge lines may indicate the stacking of a few single crystalline nanosheets, at least in the nearly 1 by 1 μm^2 large view area in Fig. 3a. The single-crystalline nanosheets can also be verified by the spot pattern in the corresponding select area electron diffraction (SAED) shown in Fig. 3b. The SAED pattern can be indexed as <111> zone diffraction, agreeing well with the simulation result in Fig. S4†. Due to the strict corresponding relation of TEM image (Fig. 3a) and SAED pattern (Fig. 3b), the side surface of the nanosheet can be indexed as $\{11\,\bar{2}\}$ facets, which can be further confirmed by the HRTEM image in Fig. 3d. Lattice spacing according to fringes in Fig. 3c is 0.35 nm, which can be attributed to the {101} planes of anatase TiO_2. The corresponding angle between the two lattice fringes is 82.2°, identifying the {116} facets as the surface of the exposed nanosheets.[9, 16] The corresponding FFT pattern of the lattice fringes shown as the inset in Fig. 3c agrees well with the SAED pattern in Fig. 3b. The vertical growth direction can be deduced from Fig. 3d and the corresponding FFT pattern as $<1\bar{1}0>$, perpendicular to the $\{1\bar{1}0\}$ facets, which coincide well with the XRD results that the (220) diffraction peak is the strongest. Comparing the FFT pattern in Fig.3d with the SAED pattern in Fig. 3b, the horizontal growth direction can be deduced as $<33\bar{1}>$, which is the normal line of $\{11\bar{2}\}$ facets, further confirming $\{11\bar{2}\}$ facets as the side surface of nanosheet. Fig. 3e shows the crystalline structure of (116) plane viewed along with its normal line [111] direction: the (116) plane lies horizontally as the top face, while $(10\bar{1})$, $(0\bar{1}1)$, $(1\bar{1}0)$ and $(\bar{1}\bar{1}2)$ planes stand vertically with specific angles, which is consistent well with the crystalline data in Fig. 3d. Magnified FESEM image in Fig. 3f corresponds to the top edge of STNA-116, and angles of the nanosheet tips are mostly larger than 120°, indicating that the side facets of the tips may be {211} facets, making (211) peak as the second strongest diffraction peak in Fig. 2a. The relationships of {101}, {110} and {211} facets are also illustrated in Fig. 3g, crystalline structure of (116) plane viewed along with its normal line [111] direction. The above SEM, XRD and HRTEM results strongly support that the nanosheets in the nanostructured array are single-crystalline anatase TiO_2 nanosheets exposed with {116} facets, and the vertical and the horizontal growth direction are $<1\bar{1}0>$ and $<33\bar{1}>$,respectively. The relationship between exposed facet and growth direction are shown in Fig. 3h.

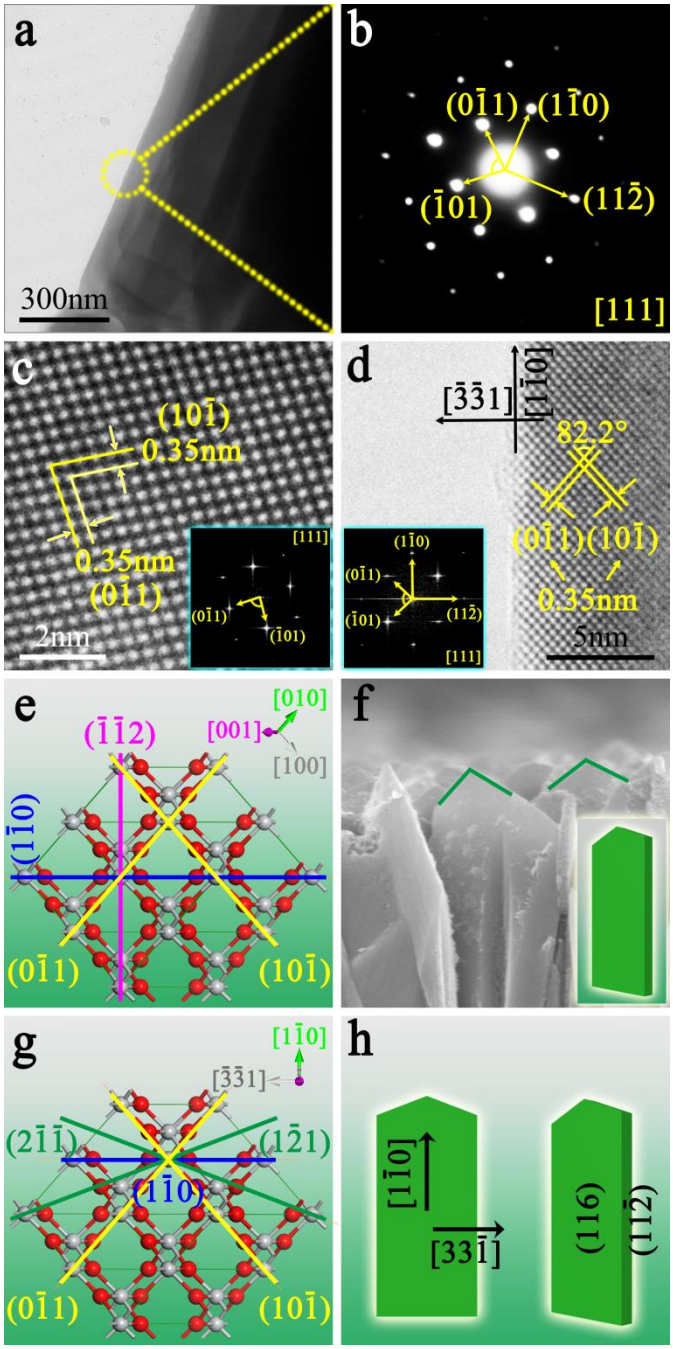

Fig. 3 (a, b) TEM images of STNA-116 building unit and the corresponding SAED pattern. (c) High resolution TEM image of STNA-116 building unit and the corresponding fast Fourier transformation pattern (bottom-right inset). (d) High resolution TEM image of STNA-116 building unit from side edge and the corresponding fast Fourier transformation pattern (bottom-left inset). (e) Crystal structure of anatase TiO_2 viewed along [111] direction, indicating that $\{1\bar{1}0\}$ (blue line), $\{\bar{1}\bar{1}2\}$ (pink line) and $\{10\bar{1}\}$ (yellow line) facets stand orthogonal to {116} facets. (f) High resolution FESEM image of STNA-116 from top edge and morphology model of the nanosheet (bottom-right inset). (g) The geometrical relationships between $[\bar{3}\bar{3}1]$, $[1\bar{1}0]$ and the specific crystal facets. (h) Structure model of nanosheet in different views.

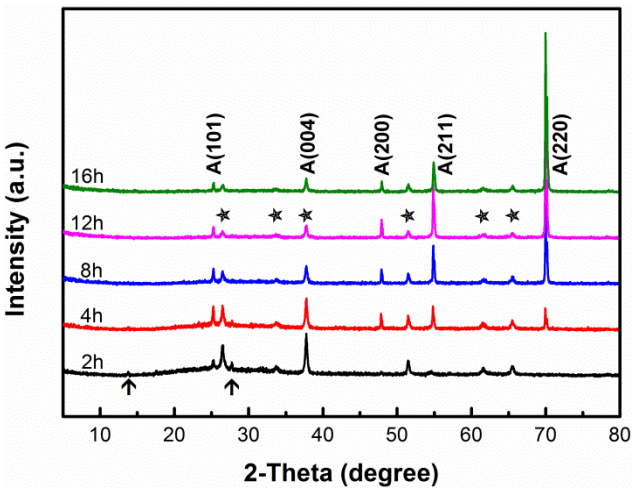

Fig. 4 XRD patterns of STNA-116 grown on FTO substrate in 15 ml ethanol, 1 ml titanium butoxide, and 1 ml hydrofluoric acid at 200 °C for 2, 4, 8, 12, and 16 h. Diffraction peaks marked with stars belong to the FTO substrate.

Time-dependent serial experiments were introduced to study the growth process of STNA-116. The concentration of the precursor in this series was doubled to strengthen the discrimination. Fig. 4 shows the XRD patterns of STNA-116 samples grown at 200 °C for a series time, and the corresponding FESEM images are shown in Fig. S5†. For the sample with the growth time of 2 h, there was no TiO_2 nanosheet observed under FESEM, and the extremely weak TiO_2 X-ray diffraction peaks in Fig. 4 belong to the TiO_2 seed layer. The diffraction peaks marked with arrows can be ascribed to hexagonal $TiOF_2$.[9] TiO_2 nanosheets with a side length of ~1.57 μm and a laminar thickness of about 30 nm grow nearly perpendicularly to the substrate after 4 hours. The nanosheets crossly support each other, keeping the fishnet-like film highly oriented to the substrate. While the laminar thicknesses remain unchanged (~ 30 nm), the side lengths of the nanosheets increase to about 3μm at 8 hours and about 4.71 μm at 12 hours, respectively. Peak intensity ratios for (101), (211) and (220) diffraction peaks of different STNA-116 are shown in Fig. 5. (211) and (220) diffraction peaks were

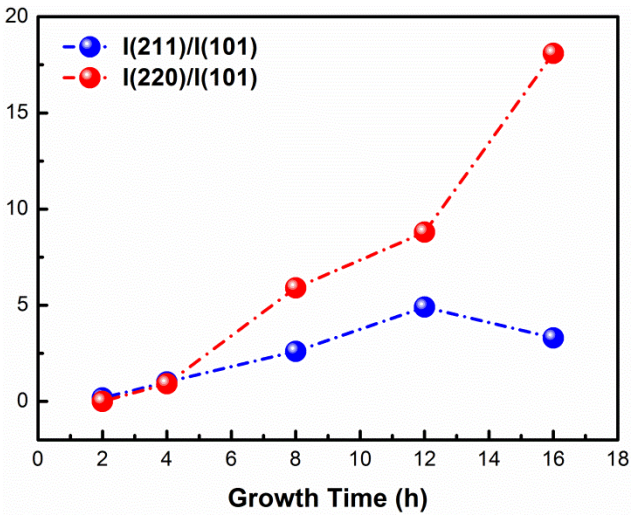

Fig. 5 Peak intensity ratios for (101), (211) and (220) diffraction peaks of STNA-116 grown for 2, 4, 8, 12 and 16 h.

enhanced significantly along with the increase of the nanosheet side length. The side length of the nanosheet of 16 hours didn't increase that much when compared to that of 12 hours, while the laminar thickness decreased slightly. This can be attributed to the exhaustion of the precursors and to the etching effect of the hydrofluoric acid. Therefore during the growth process, the laminar thickness of the nanosheet reached to ~ 30 nm quickly and remained almost unchanged with the growth time. The side length, however, kept increasing until the exhaustion of the precursor.

A detailed description over the formation mechanism for the {116} facets exposed nanosheets would be difficult, due to that the alcohol-thermal process is indeed complicated and is difficult to be monitored in situ. Here a simple mechanism was assumed: In our alcohol-thermal reaction system, ethanol was taken as the solvent and titanium butoxide was used as the titanium precursor. The high concentration of hydrofluoric acid inhibited the hydrolysis of titanium precursor in the solution, which was demonstrated for there was no TiO_2 powder obtained in the ethanol solution. However, there generally exists a boundary layer between liquid and solid, and the concentration of each component in the boundary layer may be quite different to that in bulk liquid, which may be more distinct in this case because of the hydrophilic TiO_2 seed crystal coated substrate. At the initial growth stage, titanium precursor reacted with H_2O/HF in the boundary layer, leading to the nucleation and the formation of hexagonal $TiOF_2$ on the substrate, as illustrated in the sample with the growth time of 2 hours. Then the hexagonal $TiOF_2$ may act as the hard template for {116}-faceted anatase, and the formation of nanosheet may result from the diffusion limited mechanism.[17] In the previously reported works,[7, 18-20] TiO_2 nanosheets synthesized by using hydrofluoric acid as the capping agent were all exposed with {001} facets. The main differences between our work and the previously reported works are the adoption of high relative concentrations of HF and ethanol solvent. As a result, F- and ethanol would absorb preferentially on the {116} facets due to the plenty of three and five-coordinated Ti atoms on the {116} facets, limiting the growth along <111> zone, and then promoting the growth along $<1\bar{1}0>$ zone. Therefore, singe-crystalline TiO_2 nanosheets exposed with {116} facets were formed. The suggested growth process of STNA-116 was also illustrated in Scheme 1.

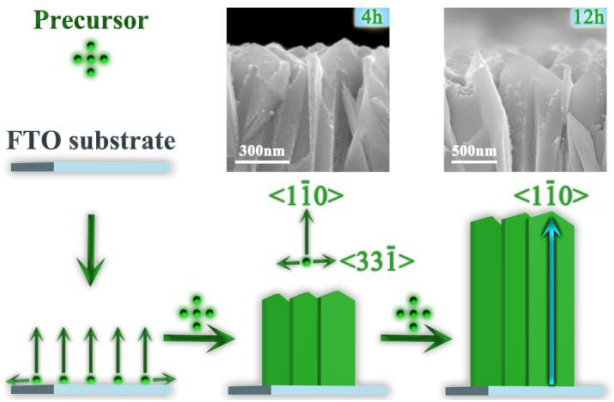

Scheme 1. Schematic drawing of the suggested growth process. Insets are corresponding FESEM images of the nanosheets from top edge.

The optical property of STNA-116 was also further investigated. Compared to P25 film, the reflectivity of STNA-116 is noticeably decreased. The wavelength at the 30% reflectivity is red-shifted by 25 nm, which can be attributed to the smaller band gap of {116} facets and corresponding a higher absorption in the ultraviolet region. The sample also exhibits a lower reflectivity of about 50% in the range of 400-800 nm, demonstrating the foreseeable light trapping effect by the nanostructures, which is common among such nanoarray structures. Corresponding light path diagrams are illustrated in the insets of Fig. S6†. The results indicate that the structure can serve as an anti-reflecting film and enhance the light harvesting efficiency, which would be helpful to future solar energy conversion applications.

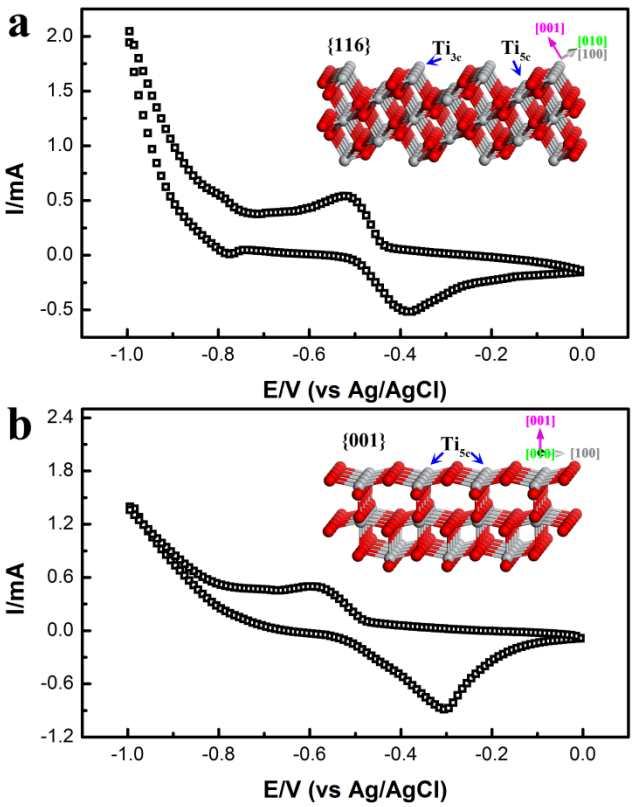

Fig. 6 Cyclic voltammograms of (a) STNA-116 and (b) STNA-001 electrode in 0.5 M H_2SO_4. Scan rate: 50 mVs^{-1}. Insets are corresponding atomic structures.

Electrochemical characterization was used here as a simple way to evaluate the STNA-116's performances. STNA-116, STNA-001 and P25 films all on FTO substrates were used as work electrodes in the electrolyte solutions. In order to make sure that the comparison was made under the similar conditions, all the samples were annealed at 500 ºC for 2 h before the electrochemical characterization. The cyclic voltammograms tested in 0.5 M H_2SO_4 at a scan rate of 50 mVs^{-1} are shown in Fig. 6. The electrochemical characteristics of the electrodes are listed in Table 1. The anodic peaks can be attributed to $Ti^{4+} + e^- \rightarrow Ti^{3+}$. Comparing with STNA-001, STNA-116 has a smaller cathodic peak potential, leading to a better reduction capacity. With a peak separation potential of 0.13 V and a ratio ipa/ipc≈1, STNA-116 exhibits a much higher electrochemical reversibility than STNA-001.[22] P25 film was also further investigated, which exhibited even larger cathodic peak potential and worse reduction capacity than that in STNA-001 (Fig. S7†). As shown in the surface atom structure in the insert of Fig. 6, compared to the {001} facets, the enhanced electrochemical performance of {116} facets can be attributed to the more favourable atomic structure, which possesses much more three, five-coordinated Ti atoms, and provides more active reaction sites for the electrochemical reactions.[23] Based on the enhanced reduction capacity and highly electrochemical reversibility, STNA-116 may present promising application potential in the photoelectrochemical field.

Table 1. Electrochemical characteristics of STNA-116 and STNA-001.

	Epa[a]/V	Epc[b]/V	Ep[c]/V	(ipa[d]/ipc[e])[f]
STNA-116	-0.385	-0.515	0.13	1.046
STNA-001	-0.305	-0.605	0.3	2.015
P25	-0.275	-0.615	0.34	2.757

[a]Anodic peak potential. [b]Cathodic peak potential. [c]Peak separation potential. [d]Anodic peak current. [e]Cathodic peak current. [f]Ratio for anodic and cathodic peak currents.

Conclusions

In summary, anatase nanosheet arrays which were self-assembled by single-crystalline anatase nanosheets exposed with {116} facets were grown with a facile alcohol-thermal route uniformly on large area FTO substrates. The {116} facets exposed single-crystalline nanosheet arrays exhibit an enhanced light trapping effect in all the investigated wavelength range, as well as significantly enhanced electrochemical performance than that with {001} facets. The research pictures at promising potential applications where efficient light generated electron and hole separation at the nanoscale is crucial. The strategy to synthesis light trapping anatase nanosheet array exposed with high-index facets provides an alternative route to engineer facets, and may be extended to other material systems, leading to a significant improvement in the performance for potential applications.

Acknowledgment

This work was supported by the National Basic Research Program of China (2012CB922000).

Notes and references

[a] CAS Key laboratory of Materials for Energy Conversion, Department of Materials Science and Engineering, University of Science and Technology of China, Hefei 230026, P. R. China.
[b] National Laboratory for Physical Sciences at the Microscale, University of Science and Technology of China, Hefei 230026, P. R. China.
[c] Synergetic Innovation Center of Quantum Information & Quantum Physics, University of Science and Technology of China, Hefei 230026, P. R. China. E-mail: fuzp@ustc.edu.cn, yllu@ustc.edu.cn.
† Electronic Supplementary Information (ESI) available: Photo of the large area STNA-116, FESEM images of STNA-001 and STNA-116 with a series of growth time, the enlarged XRD pattern, the simulated SAED pattern, the reflectance spectra, the cyclic voltammograms of P25 on FTO substrate are included in the supporting information. See DOI: 10.1039/c000000x/

1 X. J. Feng, K. Shankar, O. K. Varghese, M. Paulose, T. J. Latempa and C. A. Grimes, *Nano Lett.*, 2008, **8**, 3781-3786.
2 A. Fujishima and K. Honda, *Nature*, 1972, **238**, 37-38.
3 S. Sangaraju and G. Aharon, *small*, 2007, **3**, 1189–1193.

4 D. H. Wang, D. W. Choi, J. Li, Z. G. Yang, Z. M. Nie, R. Kou, D. H. Hu, C. M. Wang, L. V. Saraf, J. G. Zhang, I. A. Aksay and J. Liu, *ACS Nano*, 2009, **3**, 907–914.
5 Q. Zheng, B. X. Zhou, J. Bai, L. H. Li, Z. J. Jin, J. L. Zhang, J. H. Li, Y. B. Liu, W. M. Cai and X. Y. Zhu, *Adv Mater*, 2008, **20**, 1044-1049.
6 T. Taguchi, Y. Saito, K. Sarukawa, T. Ohno and M. Matsumura, *New J Chem*, 2003, **27**, 1304-1306.
7 H. G. Yang, C. H. Sun, S. Z. Qiao, J. Zou, G. Liu, S. C. Smith, H. M. Cheng and G. Q. Lu, *Nature*, 2008, **453**, 638-641.
8 H. B. Wu, J. S. Chen, X. W. Lou and H. H. Hng, *Nanoscale*, 2011, **3**, 4082-4084.
9 F. Li, J. Xu, L. Chen, B. B. Ni, X. N. Li, Z. P. Fu and Y. L. Lu, *J Mater Chem A*, 2013, **1**, 225-228.
10 C. Battaglia, J. Escarre, K. Soderstrom, M. Charriere, M. Despeisse, F. J. Haug and C. Ballif, *Nat Photonics*, 2011, **5**, 535-538.
11 B. Liu and E. S. Aydil, *J Am Chem Soc*, 2009, **131**, 3985-3990.
12 A. Polman and H. A. Atwater, *Nat Mater*, 2012, **11**, 174-177.
13 W. Wang, S. M. Wu, K. Reinhardt, Y. L. Lu and S. C. Chen, *Nano Lett.*, 2010, **10**, 2012-2018.
14 S. L. Feng, J. Y. Yang, H. Zhu, M. Liu, J. S. Zhang, J. Wu and J. Y. Wan, *J Am Ceram Soc*, 2011, **94**, 310-315.
15 W. X. Guo, F. Zhang, C. J. Lin and Z. L. Wang, *Adv Mater*, 2012, **24**, 4761-4764.
16 Y. Z. Jiao, C. X. Peng, F. F. Guo, Z. H. Bao, J. H. Yang, L. Schmidt-Mende, R. Dunbar, Y. Qin and Z. F. Deng, *J Phys Chem C*, 2011, **115**, 6405-6409.
17 C. Li, L. Huang, G. P. Snigdha, Y. F. Yu and L. Y. Cao, *ACS Nano*, 2012, **6**, 8868-8877.
18 S. J. Ding, J. S. Chen, Z. Y. Wang, Y. L. Cheah, S. Madhavi, X. A. Hu and X. W. Lou, *J Mater Chem*, 2011, **21**, 1677-1680.
19 W. Q. Fang, J. Z. Zhou, J. Liu, Z. G. Chen, C. Yang, C. H. Sun, G. R. Qian, J. Zou, S. Z. Qiao and H. G. Yang, *Chem-Eur J*, 2011, **17**, 1423-1427.
20 W. G. Yang, J. M. Li, Y. L. Wang, F. Zhu, W. M. Shi, F. R. Wan and D. S. Xu, *Chem Commun*, 2011, **47**, 1809-1811.
21 S. Mokkapati and K. R. Catchpole, *J Appl Phys*, 2012, **112**.
22 J. Heinze, *Angew Chem Int Edit*, 1984, **23**, 831-847.
23 H. Xu, P. Reunchan, S. X. Ouyang, H. Tong, N. Umezawa, T. Kako and J. H. Ye, *Chem Mater*, 2013, **25**, 405-411.